Initial Observations of VLF Electric and Magnetic Fields with the Injun 5 Satellite

DONALD A. GURNETT, G. WILLIAM PFEIFFER, ROGER R. ANDERSON, STEPHEN R. MOSIER,[1] AND DAVID P. CAUFFMAN

Department of Physics and Astronomy
The University of Iowa
Iowa City, Iowa 52240

The Injun 5 satellite, launched into a low-altitude (677–2528 km) polar orbit on August 8, 1968, carried a very-low-frequency (VLF) electric and magnetic fields experiment covering the frequency range from dc to 105 kHz for electric fields and from 30 Hz to 10 kHz for magnetic fields. This paper describes the VLF experiment and presents initial results of immediate interest. Broadband (30 Hz to 10 kHz) electric field intensities are found to be remarkably small, typically less than 100 μv/m and seldom greater than 1 mv/m. Most of the common types of VLF electromagnetic noise, electron and proton whistlers, chorus, ELF hiss, VLF hiss, and periodic emissions, have been observed simultaneously with both the electric and magnetic antennas, thus providing an excellent check on the operation of the electric antenna. Phase measurements between the electric and magnetic fields have been used to determine the direction of propagation, up or down the geomagnetic field. New phenomena observed include (1) spin modulation of lower hybrid resonance noise, (2) multiple frequency noise bands possibly related to lower hybrid resonance noise, (3) a narrow bandwidth electric field enhancement near the two-ion cutoff frequency, and (4) noise bands associated with harmonics of the proton gyrofrequency.

1. INTRODUCTION

This paper reports on initial results from the very-low-frequency (VLF) electric and magnetic fields experiment on the NASA/University of Iowa Injun 5 satellite. This satellite was launched on August 8, 1968, into an elliptical polar orbit with an inclination of 80.66°, an apogee altitude of 2528 km, and a perigee altitude of 677 km. The experiments on board Injun 5 included a VLF electric and magnetic fields experiment, a dc electric field experiment, a set of low-energy proton and electron differential energy analyzers (LEPEDEA) of the type described by *Frank* [1967], an array of solid-state high-energy electron and proton detectors, and an electron concentration and temperature probe.

The purpose of this paper is to describe the Injun 5 VLF experiment and to present preliminary findings of immediate interest. Since the results presented represent only a brief study of the data available, it is expected that more comprehensive studies of the various phenomena discussed will be published as more extensive analyses are completed.

2. DESCRIPTION OF THE EXPERIMENT

The principal new technical features of the Injun 5 VLF experiment include (1) the capability of simultaneously receiving both the electric and magnetic fields of plasma wave phenomena over a broad range of frequencies, from 30 Hz to 10kHz, (2) the determination of the sense of the Poynting flux, up or down the geomagnetic field, from the relative phase of the electric and magnetic field signals, and (3) the measurement of the impedance of the electric antenna to help verify our understanding of the electric antenna operation.

The VLF experiment instrumentation consists of one electric dipole antenna, one magetic loop antenna, two wide-band (30 Hz to 10 kHz) receivers, a narrow-band step-frequency receiver, and an impedance measurement for determining the electric antenna impedance. The position and orientation of the two VLF antennas on the spacecraft are shown in Figure 1. The electric dipole antenna, whose axis is parallel to the y axis of the spacecraft, is of the

[1] NASA Graduate Trainee.

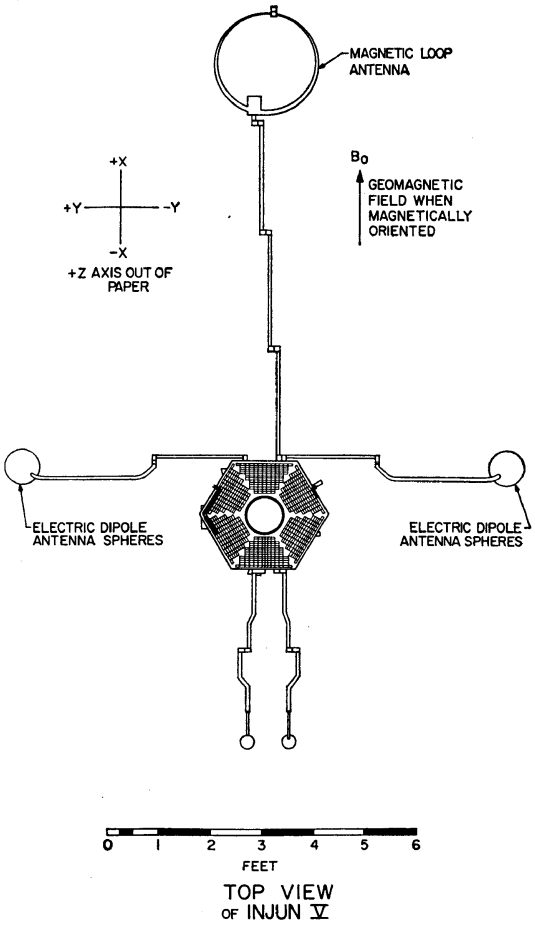

Fig. 1. Location and orientation of the VLF antennas on the spacecraft.

type described by *Storey* [1965] and consists of two spherical aluminum antenna elements 20.3 cm in diameter with a center-to-center separation of 2.85 meters. The aluminum booms supporting these antenna elements are insulated from the spheres and from the spacecraft body and are coated with a nonconducting paint to insulate the booms from the surrounding plasma.

The magnetic loop antenna, whose axis is parallel to the z axis of the spacecraft, consists of 6 turns of number 14 copper wire wound on a circular form 0.56 meter in diameter. The loop wires are electrostatically shielded to prevent the detection of ambient electrostatic waves (which have no magnetic field). The loop antenna is located on the end of a boom to reduce interference generated by the spacecraft to an acceptable level.

The spacecraft is magnetically oriented by a bar magnet within the spacecraft such that, when properly aligned, the x axis of the spacecraft is parallel to the geomagnetic field with the positive x axis downward in the northern hemisphere. When the spacecraft is magnetically aligned, the electric antenna axis and the magnetic antenna axis are perpendicular to the geomagnetic field as well as to each other. This antenna geometry was chosen so that the direction of the Poynting flux of an electromagnetic wave, up or down the geomagnetic field, can be determined from the relative phase between the electric and magnetic antenna signals (see section 5 for a further discussion of the Poynting flux determination).

A block diagram of the VLF experiment electronics is shown in Figure 2. The electric antenna preamplifiers are high input impedance unity gain amplifiers and are located inside the spherical antenna elements. The input impedance of the unity gain preamplifiers can be represented by a 20-megohm resistor, R_b, in parallel with a 10-pf capacitance, C_{in} (the input shunt capacitance of the preamplifier). The noise level of the unity gain preamplifiers is about 10^{-14} volt^2 Hz^{-1}. The unity gain preamplifiers provide signals, by means of coaxial cables inside the booms, to a differential amplifier in the main electronics package. The unity gain preamplifiers also drive the aluminum booms supporting the spheres to reduce the sphere-boom capacity. The output of the differential amplifier is proportional to the potential difference, hence electric field, between the two spheres.

In a special mode of operation, controlled by command, the spheres can be biased with a 1-μamp current source (E_b = 20 volts across R_b = 20 megohms, see Figure 2) to study the effects of bias currents on the antenna operation. The electrons collected by the spheres when in the bias mode of operation are returned to the surrounding plasma by a collimated hot filament labeled 'electron gun' in Figure 2. The electron gun is located at the end of the loop antenna boom.

The impedance of the electric antenna is measured periodically by differentially driving the antenna elements with a constant ampli-

tude ac current source ($I = 0.1$ μamp rms) whose frequency decreases exponentially in time from 20 kHz to 20 Hz. The ratio of ac potential difference between the spheres V, from the differential amplifier, to the current I, gives the magnitude of the antenna impedance $|Z| = V/I$, and a comparison of the voltage and current waveforms gives the phase Φ of the impedance. An impedance measurement is made every 30 seconds, each impedance sweep requiring 8 seconds, 2 seconds to stabilize, and 2 seconds per decade from 20 kHz to 20 Hz. The magnitude measurement has a dynamic range from about 5 kilohms to 10 megohms, and the phase measurement has a dynamic range of $\pm 90°$.

The dc potential of the electric antenna spheres is continuously monitored to study dc electric fields, to detect changes in the bias condition of the spheres due to wake effects, variations in the photoelectron current emitted by the spheres (shadowing, sunrise and sunset effects, etc.), and to investigate the effects of bias variations on the antenna impedance and operation. Two measurements of the dc sphere potentials are performed. First, the average dc potential of the spheres relative to the spacecraft potential is transmitted every 30 seconds over a dynamic range of -10.0 to $+10.0$ volts. Second, the dc potential difference between the spheres is transmitted every 4 seconds over a dynamic range of -1.0 to $+1.0$ volts. The input impedance of the amplifier used to make these dc potential measurements is 40 megohms, and the time constant is about 1.0 second.

The ac signals from the electric antenna differential amplifier go to a narrow-band step-frequency receiver and to a wide-band receiver (see Figure 2). The step-frequency receiver has six frequency channels, 7.50, 10.5, 22.0, 52.5, 70.0, and 105 kHz, with bandwidths of $\pm 7\frac{1}{2}\%$. The noise intensities in these channels are sampled by the digital telemetry with a time resolution of 4 seconds for the 7.5- and 10.5-kHz channels and 8 seconds for the remaining channels. The sensitivity of the step-frequency receiver is about 10^{-11} volts^2 Hz^{-1}, and the dynamic range is 60 db.

The wide-band receiver consists of two bandpass filters, each followed by a nonlinear compressor amplifier. These bandpass filters provide a low-frequency band of 30 Hz to 650 Hz and a high frequency band of 300 Hz to 10 kHz, which are independent of each other. These frequency bands are called the 'low' and 'high' bands, respectively. The nonlinear compressor amplifiers compress the dynamic range of the broad-band analog ac signals from the antenna (80 db) to a dynamic range (20 db) suitable for direct

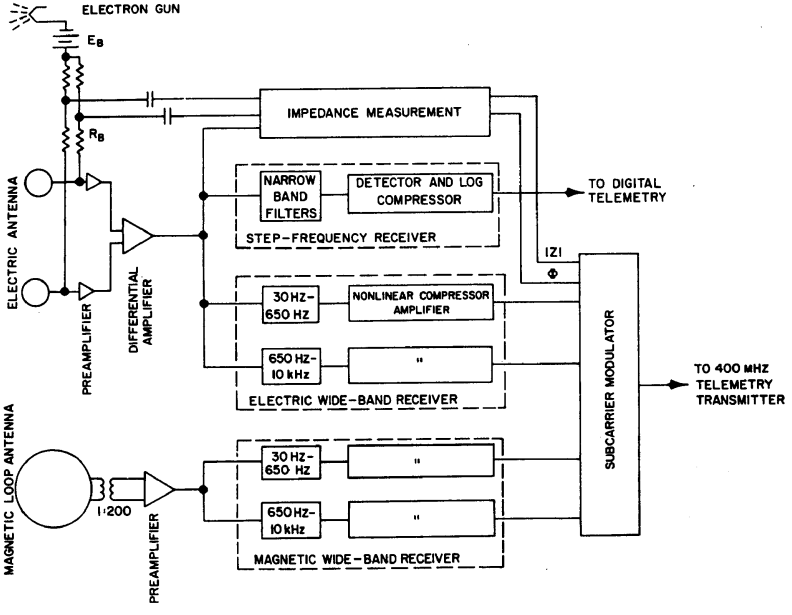

Fig. 2. Block diagram of the VLF experiment.

transmission to the ground with a 400-MHz telemetry transmitter. The wide-band receiver also provides voltages proportional to the signal amplitude in each band with a dynamic range of 80 db and a time constant of 0.25 second. These amplitude voltages are transmitted by means of the digital telemetry at a rate of one sample per second. The sensitivities of the 'high' and 'low' band amplitude measurements are both about 10 μvolts rms potential difference between the spheres.

The magnetic loop antenna is matched to the magnetic preamplifier by a transformer with a 1:200 turns ratio. The voltage from the magnetic loop, which is proportional to the time-rate of change of the magnetic field, is integrated to provide a signal proportional to the ac magnetic field. The magnetic field signal goes to a wide-band receiver identical in characteristics to the electric wide-band receiver. The sensitivities of the magnetic 'high' and 'low' bands are approximately 0.5 and 3.0 mγ, respectively (1 mγ = 10^{-8} gauss).

All of the four wide-band analog channels are transmitted simultaneously with a single 0.8 watt 400-MHz telemetry transmitter. The magnetic high band (300 Hz to 10 kHz) directly modulates the transmitter. The electric high band (300 Hz to 10 kHz) is transmitted as a single sideband subcarrier from 15.3 to 25.0 kHz, together with the 15.0 kHz single sideband carrier as a phase reference. The electric and magnetic low bands (30 Hz to 650 Hz) are transmitted as frequency-modulated subcarriers at 33.5 $\pm$ 3.5 kHz and 43.5 $\pm$ 3.5 kHz, respectively.

3. Spacecraft Operation in Orbit

A failure in the main spacecraft power regulator early in the flight resulted in somewhat reduced operation because of spacecraft power limitations. Nevertheless, large quantities of data are being obtained from all the experiments on board. Approximately 3 hours of wide-band VLF data are being obtained daily from the VLF experiment, and at the time of this report (April 1969) approximately 8 months of data have been accumulated.

Magnetic alignment was not achieved until about four months after launch (mid-December 1968) because of the rotational kinetic energy imparted to the spacecraft at launch. Typical maximum alignment errors between the x axis and the geomagnetic field after mid-December are about 10° to 15°.

The operation of the VLF experiment in orbit has been entirely satisfactory with the exception of the electron gun. The operation of the electron gun has proven to be marginal because the current emitted by the electron gun is apparently less than the 2 μamps required to bias the electric antenna spheres. The reason for the low emission current has not been established although the probable cause is believed to be contamination of the carbonate filament coating, either before launch or from oxygen poisoning while in orbit. Although the electron gun failure reduces the capability of studying the antenna operation under different bias conditions, this failure in no way affects the normal operation or performance of the experiment.

4. Electric Antenna Performance

A. Theory of operation. The theory of operation for a two-sphere electric antenna of the type used on Injun 5 has been discussed by *Storey* [1965] and *Fahleson* [1966], and is summarized here for comparison with the observed operation in orbit. From a simplified viewpoint the two-sphere antenna can be thought of as two high-impedance potential probes immersed in the highly conducting plasma surrounding the spacecraft. As is well known, when an object is placed in a plasma an inhomogeneous sheath region forms around the object. In the altitude range of the Injun 5 orbit the sheath is normally a positive ion sheath with a characteristic thickness given by the Debye length, $\lambda_D = 6.9\ (T_e/n_e)^{1/2}$ (cm), where T_e is the electron temperature (°K) and n_e is the electron number density (cm^{-3}). A small signal equivalent circuit model of the coupling of the antenna elements to the surrounding plasma, through the sheath, is shown in Figure 3. The sheath resistance, R_s, can be estimated from Langmuir probe theory and for a Maxwellian electron velocity distribution is approximately [*Storey*, 1965]

$$R_s = \frac{U_e}{I_i + I_p} \qquad U_e = \frac{kT_e}{e}$$

where U_e is the electron thermal energy (volts), I_i is the ion current incident on the antenna, and I_p is the photoelectron current emitted by

antenna. Typical values for R_s for the Injun orbit and sphere size range from about 10^4 to 10^7 ohms. The sheath capacity, C_s, can be estimated from the capacitance between the antenna and the plasma assuming that the sheath region has a dielectric constant of unity. Typical values for C_s vary from the free space capacity of the spheres (11 pf) in regions of low electron concentration (large λ_D) to about 100 pf in regions of high electron concentration near perigee.

Except near characteristic resonance frequencies of the plasma, the bulk impedance of the plasma between the spheres is expected to be much less than the sheath impedance [*Harvey*, 1965]. Therefore, in the equivalent circuit model shown in Figure 3 only the sheath impedance is included. Since the sheath impedances are strongly dependent on the local plasma parameters, it is desirable to make the determination of the plasma potential Φ independent of the sheath impedance. From the equivalent circuit model in Figure 3, it is evident that this condition can be realized only if the preamplifier input impedance is comparable to, or larger than, the sheath impedance at all frequencies of interest, or equivalently, $R_b \gtrsim R_s$ and $C_{in} \lesssim C_s$. The Injun 5 preamplifiers, with $R_b = 20$ megohms and $C_{in} = 10$ pf, satisfy these inequalities for most plasma densities and temperatures expected. The inflight electric antenna impedance measurement provides a direct verification that the antenna impedance is, in fact, less than the preamplifier input impedance.

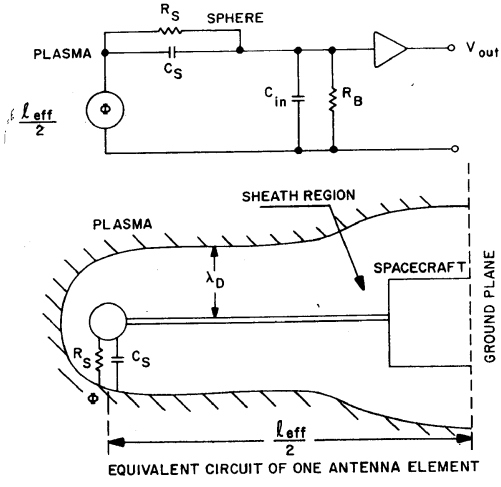

Fig. 3. Equivalent circuit of one antenna element.

The effective length of the antenna, l_{eff}, shown in Figure 3, is the ratio of the potential, Φ, to the electric field component, E, parallel to the antenna. When the sheath thickness (Debye length) is small compared with the distance between the spheres, it is clear that the effective length is very nearly equal to the distance between the spheres because the coupling to the plasma through the sheath takes place very close to the spheres. As the Debye length becomes large compared with the distance between the spheres, the effective length approaches the free space value, which is slightly different from the physical distance between the spheres because of the induced polarization charges on the spacecraft and the booms. The effective length can be determined in flight by comparing the electric and magnetic field amplitudes of an electromagnetic wave for which the ratio of E to B is known.

B. Observed antenna impedance. A typical in-flight electric antenna impedance measurement is illustrated in Figure 4. As shown in the frequency-time spectrogram at the top of Figure 4, the impedance data are transmitted in the electric wide-band telemetry channel as tones whose frequencies are proportional to the phase and magnitude of the antenna impedance. The frequency-time spectrogram in Figure 4 also shows the frequency sweep as a frequency exponentially decreasing with time. The impedance magnitude and phase angle, appropriately scaled from the frequency-time spectrogram, are shown as a function of the sweep frequency by the solid curves at the bottom of Figure 4. The impedance is seen to vary monotonically with frequency, from capacitive (−60° phase angle) at 20 kHz to resistive (0° phase angle) at frequencies below about 200 Hz. Qualitatively, the frequency dependence of the antenna impedance is similar to the frequency dependence expected for the simple parallel resistor-capacitor sheath impedance model illustrated in Figure 3. For comparison the dashed curves in Figure 4 show the impedance variation expected for a sheath resistance of $R_s = 2.6$ megohms and a sheath capacitance of $C_s = 15$ pf. Note that no significant impedance effect is evident at the lower hybrid resonance [*Stix*, 1962] frequency, f_{LHR}, of the ambient plasma.

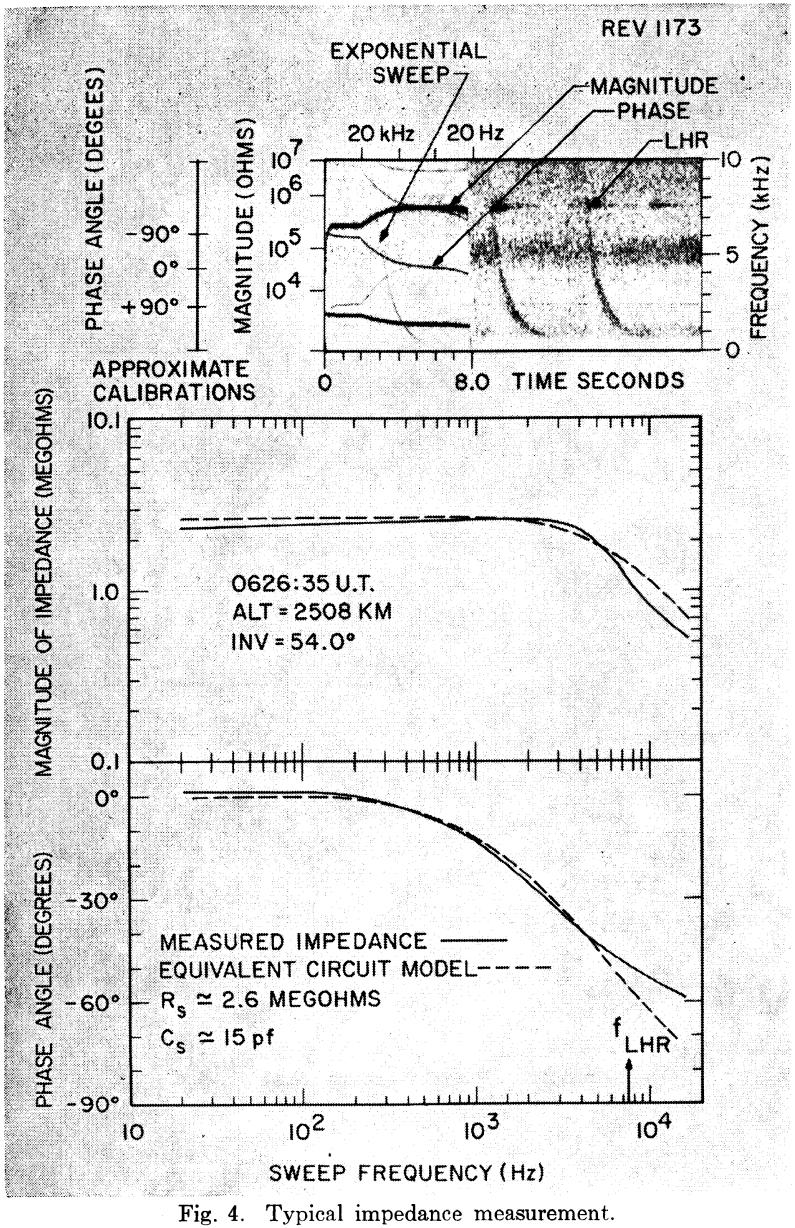

Fig. 4. Typical impedance measurement.

The LHR frequency was determined from the reflection of whistlers at the LHR frequency [see the discussion in section 7].

The impedance measurement illustrated in Figure 4 is typical of the impedances generally observed with Injun 5. Although small (~20%) deviations from the resistor-capacitor sheath impedance model sometimes occur, no evidence of marked variations in the antenna impedance have been found at any of the characteristic resonance or cutoff frequencies of the ambient plasma. Thus, the sheath impedance is the dominant impedance observed.

The sheath capacitance and, particularly, the sheath resistance are observed to vary widely during an orbit. The sheath capacitance, C_s, varies from about 15 pf at high altitudes near apogee to about 50 pf at low altitudes near perigee. The sheath resistance, R_s, has been observed to vary from about 10^7 ohms at high

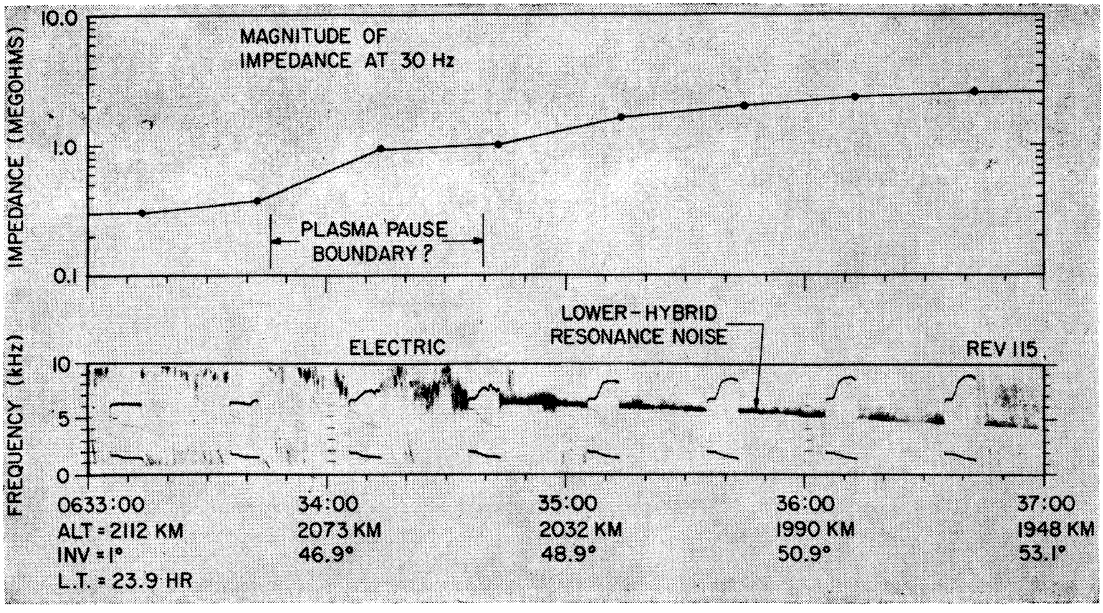

Fig. 5. Impedance change at the plasmapause.

altitudes (2500 km) over the polar region to less than 10^4 ohms at low altitudes (800 km) near the magnetic equator. These sheath impedances are in reasonably good quantitative agreement with values expected from the sheath impedance models of *Storey* [1965] and *Fahleson* [1967] for representative ionospheric parameters.

Particularly repeatable antenna impedance variations are observed near the plasmapause and the magnetic equator. Figure 5 illustrates the rapid change in the sheath resistance ($R_s \simeq$ impedance magnitude at 30 Hz) commonly observed as the satellite crosses the plasmapause boundary. The plasmapause in this case can be located approximately (plus or minus about 30 seconds) by the rapid decrease and fluctuations of the LHR noise band at the plasmapause boundary [*Carpenter et al.*, 1968]. This characteristic increase in the sheath resistance,

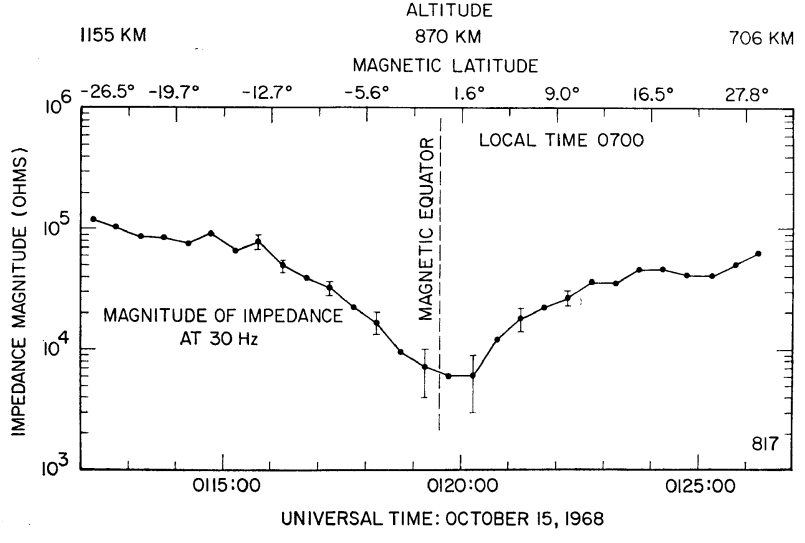

Fig. 6. Impedance minimum near the magnetic equator.

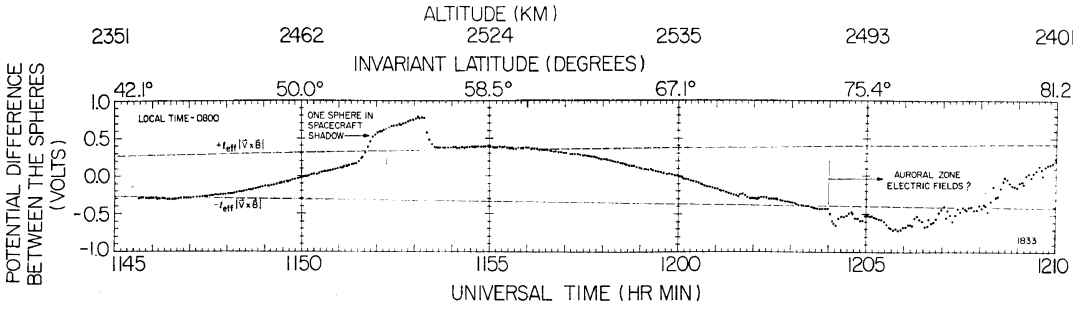

Fig. 7. The dc potential difference between the spheres compared with the **V × B** potential difference (dotted lines).

$R_s = T_e/(I_i + I_p)$, is believed to be due to the increase in the plasma temperature, T_e, and the decrease in the electron concentration, n_e, ($I_i \propto n_e$) as the plasmapause boundary is crossed. Figure 6 illustrates the marked decrease in the sheath resistance commonly observed at low altitudes near the magnetic equator. This decrease is believed to be due, at least in part, to the pronounced maximum in the electron concentration at the magnetic equator during local daytime [*Brace et al.*, 1967].

C. dc electric field measurements. The dc potential difference between the electric antenna spheres is shown in Figure 7 for a typical mid-latitude pass. The satellite in this case was magnetically oriented so that the electric antenna axis is perpendicular to the geomagnetic field, to within about ±10°. The systematic sinusoidal variation evident in Figure 7, with a period of about 20 minutes, is due to the **V × B** electric field from the satellite motion through the ionosphere. The sinusoidal modulation of the **V × B** potential is caused by the slow rotation of the satellite and the electric antenna axis around the geomagnetic field with a period of about 20 minutes. The dashed lines in Figure 7 are the product of the separation distance between the spheres (effective length, l_{eff} = 2.85 meters) and the magnitude of the **V × B** electric field as computed from the satellite orbit. As can be seen from Figure 7 the maximum and minimum sphere potential differences agree very well (±2%) with the computed **V × B** potential. This close agreement demonstrates that the two-sphere antenna system on Injun 5 is accurately measuring the **V × B** electric field and that the effective length for the dc electric field measurement is very close to the separation distance between the spheres.

The abrupt, 0.3-volt increase in the sphere potential difference from 1152 to 1153 UT in Figure 7 is due to the change in the photoelectron emissions of one of the spheres as the sphere passes through the optical shadow of the spacecraft body. The sheath resistance is also observed to increase by about a factor of 2 as the sphere passes through the shadow.

Starting at about 1204 UT and 73° invariant latitude in Figure 7, pronounced perturbations from the **V × B** electric field are observed. These perturbations, typically of the order of 30 mv/m, occur on virtually every pass through the auroral zone. The preliminary interpretation of these perturbations is that they are due to ionospheric electric fields. This interpretation will be discussed in more detail in a separate paper.

D. Comparison with the magnetic antenna. Virtually all the well-known types of electromagnetic VLF radio noise (electron and ion whistlers, chorus, ELF hiss, and VLF hiss) have been detected simultaneously with the electric and magnetic antennas. Preflight measurements show that the electrical coupling between the electric and magnetic receivers is less than −60 db on a free space basis ($E/cB = 1$), and that in-flight observations of impedance sweeps, which occur on the electric antenna only, and the near field of magnetic interference from the spacecraft, which is much stronger on the magnetic antenna, verify that the coupling between the two channels is negligible. Thus, the simultaneous observation of the same radio noise phenomena with both the electric and magnetic antennas leaves no doubt that the electric antenna is, in fact, detecting the electric field of electromagnetic waves.

The assumption that the effective length,

l_{eff}, is equal to the separation distance between the spheres can be checked by comparing the observed electric and magnetic field amplitudes with Maxwell's equation $\mathbf{n} \times \mathbf{E} = c\mathbf{B}$, where $\mathbf{n}$ is the refractive index vector [*Stix*, 1962]. A check of the effective length has been done for the ELF hiss example illustrated in Figure 8. ELF hiss is a commonly occurring whistler-mode electromagnetic noise found at middle to high latitudes during local daytime [*Gurnett*, 1968]. As discussed in the next section, the wave normal direction of the ELF hiss illustrated in Figure 8 is believed to be nearly parallel ($\pm 20°$) to the geomagnetic field. For wave normal directions parallel to the geomagnetic field, it is easily shown that $\mathbf{n}$, $\mathbf{B}$, and $\mathbf{E}$ are mutually orthogonal [*Stix*, 1962] so that the refractive index (from Maxwell's equation) is proportional to the ratio of the magnetic and electric field amplitudes, $n = cB/E$. The rms low-band electric and magnetic field amplitudes of the ELF hiss in Figure 8 are $B = 0.16$ gamma $\pm$ 10% and $E = 0.6$ mv/m $\pm$ 10% (using $l_{eff} = 2.85$ meters), respectively. These field strengths give a refractive index of $n \simeq 80$. For comparison, the refractive index can be independently computed from the whistler-mode refractive index equation [*Helliwell*, 1965] for

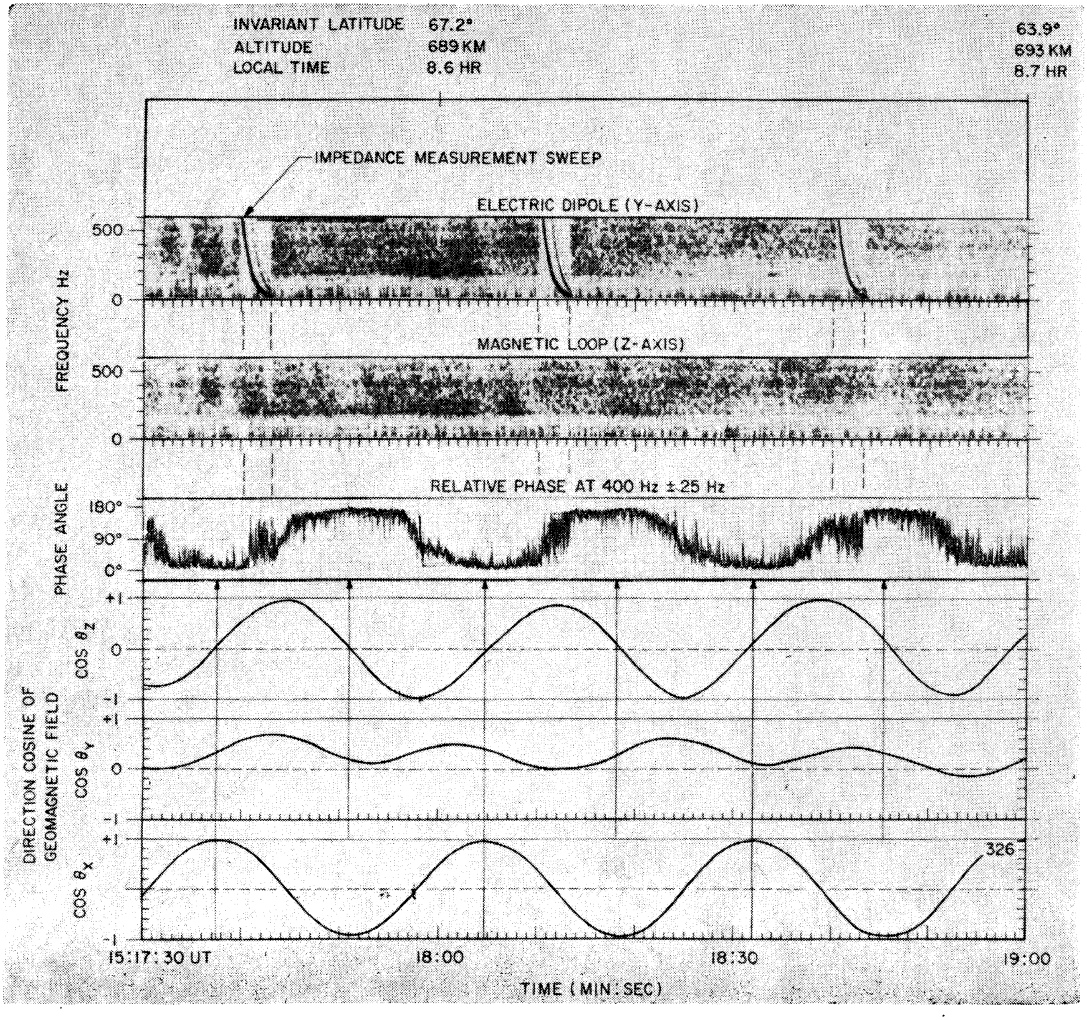

Fig. 8. Electric and magnetic field frequency spectra of ELF hiss, the phase angle between the electric and magnetic fields, and the direction cosines of the geomagnetic field (spacecraft *not* magnetically stabilized).

propagation parallel to the geomagnetic field

$$n^2 = 1 - \frac{f_{pe}^2}{f(f - f_{ge})}$$

where f is the wave frequency, f_{pe} is the electron plasma frequency, and f_{ge} is the electron gyrofrequency. The electron gyrofrequency as determined from the *Jensen and Cain* [1962] expansion for the geomagnetic field, is $f_{ge} = 1.26 \times 10^6$ Hz $\pm$ 1% and the electron plasma frequency, as determined from the AFCRL electron concentration probe on Injun 5 (R. Sagalyn, personal communication), is $f_p = 2.15 \times 10^6$ Hz $\pm$ 20%. For a wave frequency of 400 Hz the refractive index computed from these parameters is $n = 95 \pm 20\%$, which agrees with the refractive index determined from the ratio of the magnetic and electric field amplitudes to within the accuracy limits of the measurements. This excellent agreement between the two methods of determining the refractive index shows that the effective length used for the electric antenna (the separation distance between the spheres) is quantitatively correct.

E. Spacecraft generated interference. In contrast with a number of other satellite ac electric field experiments, there is essentially no detectable electric field interference from the Injun 5 spacecraft. Also, no change in the interference level is observed when the spacecraft enters the sunlight, as has been reported by several experimenters [*Osborne et al.*, 1967; *Scarf et al.*, 1968; *Laaspere et al.*, 1969]. The low level of electric field interference on Injun 5 is due to several factors. First, the noise voltages on the solar array due to power supplies, etc., are reduced to very low levels (less than 1 mv rms from 20 Hz to 1 kHz and less than 100 μv from 1 kHz to 30 kHz) by filtering the power lines going from the spacecraft electronics to the solar array. Second, the balanced dipole antenna, with a common mode rejection of about -40 db, strongly attenuates interference signals, such as solar array noise voltages, which cause the spacecraft potential to fluctuate relative to the plasma potential. Finally, extensive testing of the entire spacecraft was performed in a low noise environment at various points during the project to identify and correct interference problems.

5. Poynting Flux Measurements

A. Theoretical basis for the measurement. Despite the considerable body of data that exists on whistler-mode noise in the magnetosphere, no direct measurements have been made to determine the source region of these noises. In most cases it is not known, independent of the emission theories concerned, whether, for example, the noise is generated at high altitudes near the equatorial plane or at low altitudes in the ionosphere. Thus, measurements of the direction of propagation, particularly whether the waves are propagating up or down the geomagnetic field, are of fundamental importance for establishing the source region of various plasma instabilities in the magnetosphere.

A magnetically oriented satellite provides an ideal platform for this type of measurement since the direction of the Poynting flux, up or down the geomagnetic field, can be determined under very general conditions using just one electric and one magnetic antenna. This result may seem surprising since it would appear that the z component of the Poynting flux, $S_z = E_x H_y - E_y H_x$ ($\mathbf{B} = \mu_0 \mathbf{H}$), requires the detection of four field components in the x-y plane. However, if the z axis is parallel to the static magnetic field, Maxwell's equations and the cold plasma equations of motion relate the field components in such a way that the sign of S_z can be determined from the measurement in the x-y plane of just one electric field component and an orthogonal magnetic field component.

To prove this result consider a wave propagating in the x-z plane at an angle θ to the static magnetic field. Let the z axis be parallel to the static magnetic field. In terms of the dielectric tensor elements S, P, and D, defined by *Stix* [1962], the fields in the x-y plane are (see *Stix* [1962], Chapter 1, equation 20, and use Maxwell's equation $\mathbf{n} \times \mathbf{E} = c\mathbf{B}$)

$$E_x = e_x \operatorname{Cos}(-\omega t) \qquad E_y = e_y \operatorname{Sin}(-\omega t)$$

$$B_x = b_x \operatorname{Sin}(-\omega t) \qquad B_y = b_y \operatorname{Cos}(-\omega t)$$

where

$$e_x = E_0 \qquad e_y = \left(\frac{D}{S - n^2}\right) E_0$$

$$b_x = \frac{-n \operatorname{Cos}\theta}{c} \left(\frac{D}{S - n^2}\right) E_0$$

$$b_y = \frac{n \operatorname{Cos} \theta}{c} \left(\frac{P}{P - n^2 \operatorname{Sin}^2 \theta} \right) E_0$$

Since the satellite coordinates (primed) may be rotated at an arbitrary and unknown angle ψ around the static magnetic field, relative to the wave vector in the x-y plane, we must transform these fields to the satellite frame of reference

$$E_{x'} = E_x \operatorname{Cos} \psi + E_y \operatorname{Sin} \psi$$

$$B_{y'} = B_y \operatorname{Cos} \psi - B_x \operatorname{Sin} \psi$$

Computing time averages, denoted by the symbol $\langle\ \rangle$, over one complete period of $\operatorname{Cos}(-\omega t)$, it is easily shown that the average Poynting flux is

$$\langle S_z \rangle = \tfrac{1}{2} E_0^2 \frac{n \operatorname{Cos} \theta}{\mu_0 c} \cdot \left[\frac{P}{P - n^2 \operatorname{Sin}^2 \theta} + \left(\frac{D}{S - n^2} \right)^2 \right]$$

and that the average of the cross product $E_{x'}H_{y'}$, which can be measured in the satellite frame of reference, is

$$\langle E_{x'} H_{y'} \rangle = \tfrac{1}{2} E_0^2 \frac{n \operatorname{Cos} \theta}{\mu_0 c} \cdot \left[\frac{P}{P - n^2 \operatorname{Sin}^2 \theta} \operatorname{Cos}^2 \psi + \left(\frac{D}{S - n^2} \right)^2 \operatorname{Sin}^2 \psi \right]$$

Comparing the above two equations, it is seen that the sign of $\langle S_z \rangle$ is the same as the sign of $\langle E_{x'}H_{y'} \rangle$, independent of the unknown angle ψ, if the sign of the bracketed term is positive. The sign of the bracketed term will be positive if $P < 0$. Since $P = 1 - f_{pe}^2/f^2$, this inequality is satisfied if the wave frequency f is less than the electron plasma frequency f_{pe}, a condition always satisfied at VLF frequencies for the Injun 5 orbit. Thus, the direction of the Poynting flux can be determined from the sign of the correlation coefficient $\langle E_{x'}B_{y'} \rangle$, or equivalently, for a narrow bandwidth signal, from the relative phase Φ between the $E_{x'}$ and $B_{y'}$, fields (for $\Phi = 0° \pm 90°$, S_z is positive and for $\Phi = 180° \pm 90°$, S_z is negative).

B. Preliminary observations. To illustrate the Poynting flux determinations possible with Injun 5, the relative phase of the electric and magnetic antenna signals have been determined for the ELF hiss shown in Figure 8. The phase measurements in this case were made by filtering the electric and magnetic antenna signals with identical filters having bandwidths of ±25 Hz and center frequencies of 400 Hz and measuring the relative phase between the filtered signals with a linear phase detector. The observed phase variations are shown in the middle graph of Figure 8. The phase detector used is linear from 0° to 180° and 0° to −180° and has the same output voltage for positive and negative phase angles, $V(\Phi) = V(-\Phi)$. Thus, phase angles from 0° to 90° and from 0° to −90°, representing Poynting fluxes in the positive x-axis direction, are mapped onto the range of output voltages labeled 0° to 90° in Figure 8, and phase angles from 90° to 180° and from −90° to −180°, representing Poynting fluxes in the negative x-axis direction, are mapped onto the range labeled 90° to 180°. The phase detector has an integration time constant of 0.1 second. (Note that the satellite coordinate system is not the same coordinate system used for the preceding Poynting flux derivations. Since the electric and magnetic fields are measured in the y- and z-axes directions, respectively, the x axis is the direction along which the Poynting flux is sensed.)

For the ELF hiss case illustrated in Figure 8, the satellite is *not* magnetically oriented. This case was chosen for discussion because the spin axis orientation is such that the x axis alternately becomes nearly parallel and antiparallel to the geomagnetic field as the satellite rotates. The geomagnetic field direction in the satellite frame of reference is given by the direction cosines in the bottom three plots of Figure 8. The phase angle between the electric and magnetic signals is seen to alternate between 0° and 180° as the x axis alternately becomes parallel ($\operatorname{Cos} \theta_x = +1$) and antiparallel ($\operatorname{Cos} \theta_x = -1$) to the geomagnetic field (indicated by arrows in Figure 8). The phase angle observed, 0° when the x axis is parallel with the geomagnetic field (downward in the northern hemisphere, where these data were obtained), indicates that the ELF hiss is propagating *downward* from a source at higher altitudes in the magnetosphere. All examples of ELF hiss investigated to date (about 10 cases) have been found to be downgoing. This result is in agreement with previous evi-

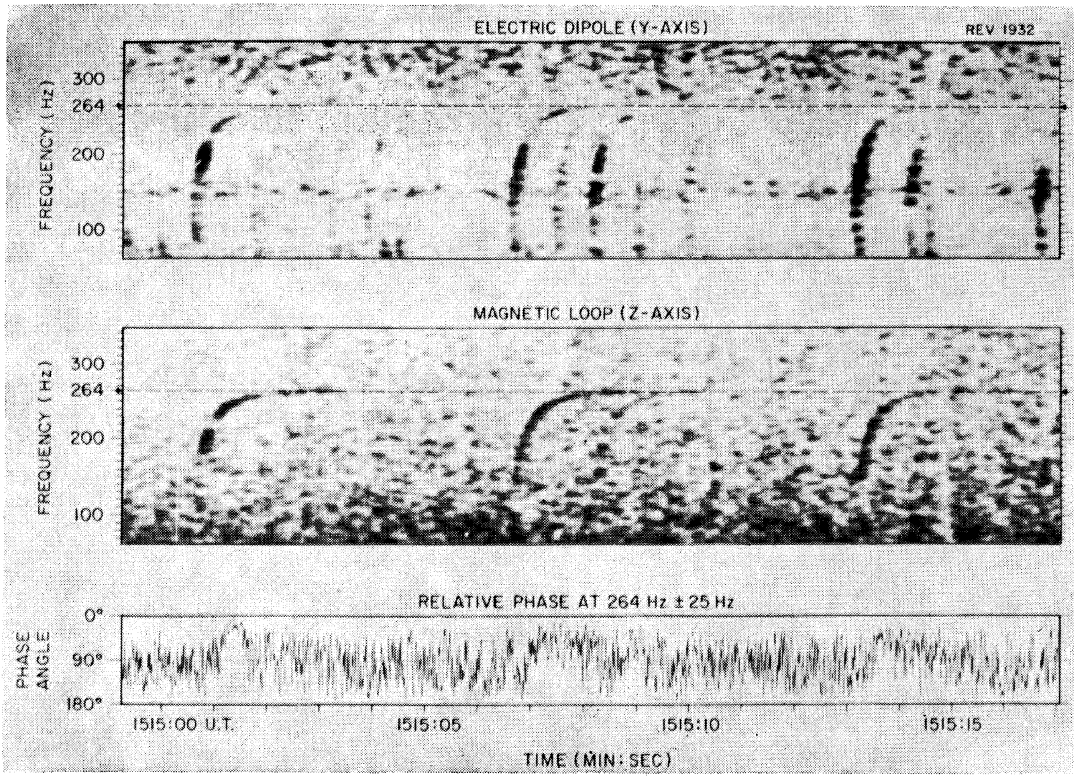

Fig. 9. Phase angle between the electric and magnetic fields for a series of proton whistlers (spacecraft magnetically oriented).

dence on the direction of propagation of ELF hiss [*Gurnett and Burns*, 1968] and consistent with instability mechanisms such as proposed by *Kennel and Petschek* [1966], which place the main source location at high altitudes near the equatorial plane.

Information about the angular distribution of wave normal directions for the ELF hiss in Figure 8 can be obtained from the spin modulation of the relative phase between the electric and magnetic antenna signals. As can be seen from Figure 8, the transition from 0° to 180° phase angle takes place rather abruptly, within about 30° of angular rotation, as the x axis becomes perpendicular to the geomagnetic field. Qualitatively, this rather sharp transition can be accounted for only if the distribution of wave normal angles for the ELF hiss is confined to a range of angles within about 15° of the geomagnetic field.

Another example, illustrating the determination of the Poynting flux for a series of proton whistlers, is shown in Figure 9. Since proton whistlers (at the latitude of this observation) are known to be propagating *upward* from the base of the ionosphere [*Gurnett et al.*, 1965], this example provides a good check on the Poynting flux sensing technique. The satellite in this case *is* magnetically stabilized so that phase comparisons can be made at any time, without regard for the orientation. The observed phase deflection when the proton whistlers occur is toward 180° phase angle, indicating that the Poynting flux is in the negative x-axis direction. Since the negative x axis of the spacecraft, when magnetically stabilized, is upward in the northern hemisphere (where these data were obtained), the proton whistler is observed to be propagating upward, as expected.

These examples of Poynting flux determinations serve to illustrate the unique capabilities of the Injun 5 Poynting flux sensing technique. This technique will be used to obtain information on the source location of chorus, VLF hiss,

and other types of VLF emissions, and to study the propagation and reflection of various whistler-mode noises in the ionosphere.

6. Representative Electric and Magnetic Field Strengths

A typical orbit of wide-band electric and magnetic field strength data is shown in Figure 10. Shown are the electric and magnetic high (0.3 to 10 kHz) and low (30 to 650 Hz) band field strengths recorded with the digital tape recorder on the satellite. The orbit shown in Figure 10 has been selected as being more or less typical of the field strengths observed with Injun 5.

The maximum magnetic field strengths observed on this orbit, 60 milligammas for the high band and 50 milligammas for the low band, are comparable to, or possibly somewhat larger than the VLF magnetic field strengths reported earlier with the Injun 3 satellite [*Gurnett and O'Brien*, 1964; *Taylor and Gurnett*, 1968]. The maxima in the magnetic field strength (also in the electric field strength), occurring symmetrically in both hemispheres during local morning at about 65° invariant latitude, are consistent with previous statistical studies [*Taylor and Gurnett*, 1968] and are believed to be primarily due to ELF hiss. Direct spectral identification of the type of noise responsible for the various field strength enhancements observed in these tape-recorded data is not possible because wide-band analog signals were not available during the periods of interest.

The maximum electric field strength observed is about 7mv/m in the high band and 3.5 mv/m in the low band. Generally, however, the wide-band electric field strengths are considerably less, of the order of 100 μv/m. For most orbits, as for the orbit shown in Figure 10, the wide-band electric field strength may be below the noise level of the preamplifier (10 μv/m) for a substantial portion of the orbit. These electric field strengths are remarkably small compared to earlier reports by *Scarf et al.* [1968].

Comparing the electric and magnetic field strength variations observed, it is evident that the field strengths often vary together, suggesting that the fields are due to electromagnetic waves, probably ELF hiss where the variations are smooth, and discrete emissions (chorus) where the fluctuations are rapid. The strong enhancement in the electric field alone, from about 2258 to 2321 UT in Figure 10, has been identified from wide-band data received during this period as high-latitude, lower hybrid resonance noise of the type described by *McEwen and Barrington* [1967].

7. New Phenomena of Special Interest

A. Lower hybrid resonance noise. An electrostatic noise band, first observed with the Alouette 1 satellite [*Barrington and Belrose*,

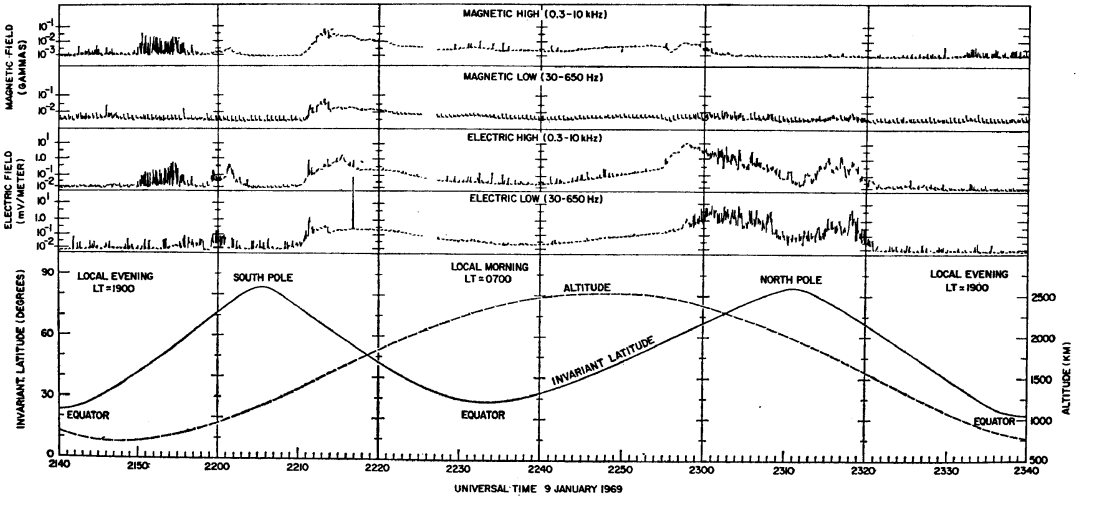

Fig. 10. Electric and magnetic field strengths observed for a typical orbit.

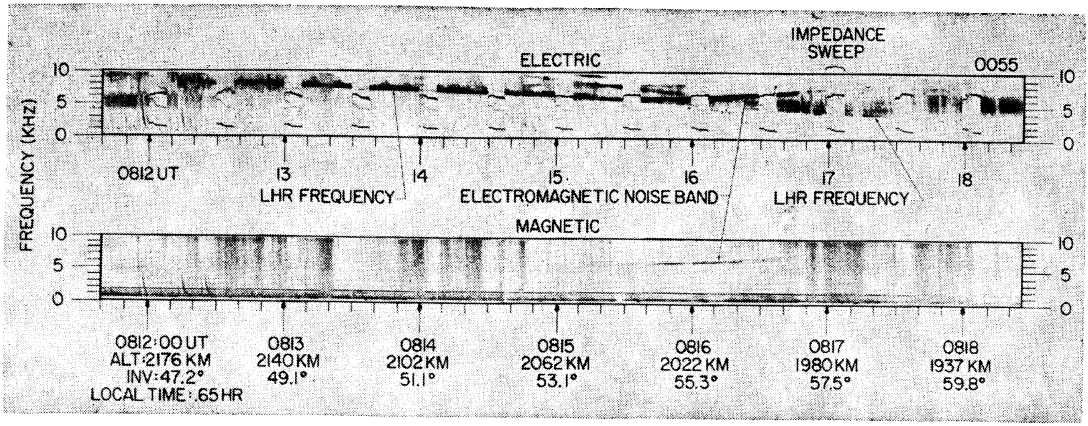

Fig. 11. Multiple noise bands, one of which is electromagnetic.

1963; *McEwen and Barrington*, 1967] and associated with the lower hybrid resonance (LHR) frequency of the ambient plasma [*Brice and Smith*, 1964, 1965], is probably the most common and most intense electric field noise observed with Injun 5. A typical example of a LHR noise band observed with Injun 5 is shown in Figure 5. The sharply defined lower cutoff frequency of the noise band is believed to be the lower hybrid resonance frequency of the ambient plasma.

Simultaneous electric and magnetic field observations with Injun 5 have confirmed earlier conclusions [*Brice and Smith*, 1965] that midlatitude LHR noise, such as illustrated in Figure 5, is almost completely electrostatic (no magnetic field). Typical high band electric field strengths for LHR noise observed with Injun 5 range from the receiver noise level up to about 10.0 mv/m. Even for the largest electric field strengths observed no magnetic component of the LHR noise has been detectable with the Injun 5 magnetic antenna. Since the sensitivity of the magnetic antenna system is about 10^{-4} gamma, for a typical bandwidth of 1 kHz, the resulting ratio of E/cB is greater than 300, indicating the LHR noise is very nearly electrostatic.

Several examples of multiple frequency noise bands, which resemble LHR noise bands in some respects, have been found in the Injun 5 data. One such case is illustrated in Figure 11, which shows several distinct electric field noise bands, one of which has a clearly defined magnetic field component. The LHR frequency in this case is believed to correspond with the lowest cutoff frequency evident in Figure 11. This identification was made by following the cutoff in question to higher latitudes where the other noise bands disappeared and the cutoff has characteristics typical of LHR noise bands commonly observed at midlatitudes. If this identification of the LHR frequency is correct, then it is clear that the frequencies of the electromagnetic noise band and the other electric field noise bands shown in Figure 11 are not related to the local LHR frequency. The merging of the electromagnetic noise band frequency with the LHR frequency at about 18h 15m 30s UT in Figure 11 suggest that the sharp upper cutoff frequency of the electromagnetic noise band may be related to the LHR frequency at some other altitude, possibly by a reflection mechanism of the type suggested by *Smith et al.* [1966] and *Storey and Cerisier* [1968].

Another new effect observed for LHR noise detected with Injun 5 is the modulation of the cutoff frequency of the noise band at the spin rate of the satellite. This spin modulation effect is illustrated in Figure 12, which shows normal (0–10 kHz) and expanded (4–10 kHz) frequency-time spectra of a LHR noise band and the angles, θ_x, θ_y, and θ_z, between the spacecraft axis and the geomagnetic field. Periodic variations of the lower, and less distinctly, the upper cutoff frequency of the LHR noise band are evident in Figure 12 at the spin period of the satellite (compare the LHR cutoff frequency variations with the orientation angles θ_x, θ_y, and θ_z).

The observed shift in the cutoff frequency of the LHR noise band is immediately sug-

gestive of a Doppler shift effect. Since the Doppler shift, $\Delta\omega = \mathbf{K}\cdot\mathbf{V}$, is dependent on the wave number ($\mathbf{K}$) direction, the observed spin modulation may be due to the rotating antenna pattern picking out waves from different directions as the satellite rotates. In some cases, in fact, the shift in the cutoff frequency can be seen to vary as Cos θ (θ is an orientation angle), strongly suggestive of the angular dependence in the Doppler shift equation, $\Delta\omega = KV$ Cos θ, where θ is the angle between $\mathbf{K}$ and $\mathbf{V}$.

Although the Doppler shift explanation is considered a very plausible explanation, another possibility also exists. It may be that the LHR noise is generated by an interaction between the spacecraft and the surrounding plasma, thus introducing an orientation dependence because of the asymmetric shape of the spacecraft body, booms, etc. At the present time the origin of the observed spin modulation is not clearly understood.

B. Electric field enhancement near the two-ion cutoff frequency. An intense very narrow bandwidth 'line' in the electric field frequency spectrum is commonly observed near the two-ion cutoff frequency in association with ELF hiss. An example of this line in the electric field frequency spectrum is illustrated in Figure 13 at a frequency slightly below the proton gyrofrequency (about 600 Hz). The frequency of this electric field enhancement is seen to be coincident with the low-frequency cutoff of the ELF hiss band evident in both the electric and, particularly, the magnetic field spectrograms. The low-frequency cutoff of the ELF hiss is due to a cutoff ($n = 0$) in the extraordinary mode of propagation, and the resulting reflection of downgoing ELF hiss, at the two-ion cutoff frequency between the proton and helium gyrofrequencies [*Gurnett and Burns*, 1968].

The observed 'line' enhancement of the electric field intensity near the two-ion cutoff frequency is believed to be due to two effects. First, the ratio of the electric-to-magnetic field amplitudes, $E/cB = 1/n$, of the ELF hiss goes to infinity very rapidly as the two-ion cutoff frequency is approached (where $n = 0$). Second, the rapid decrease in the group velocity near the reflection point causes the energy density of the wave (which is mainly in the electric field) to increase as the reflection point is approached. These two effects can, therefore, cause a strong enhancement of the electric field of the ELF hiss near the two-ion cutoff frequency. If this explanation is correct, the observed electric field

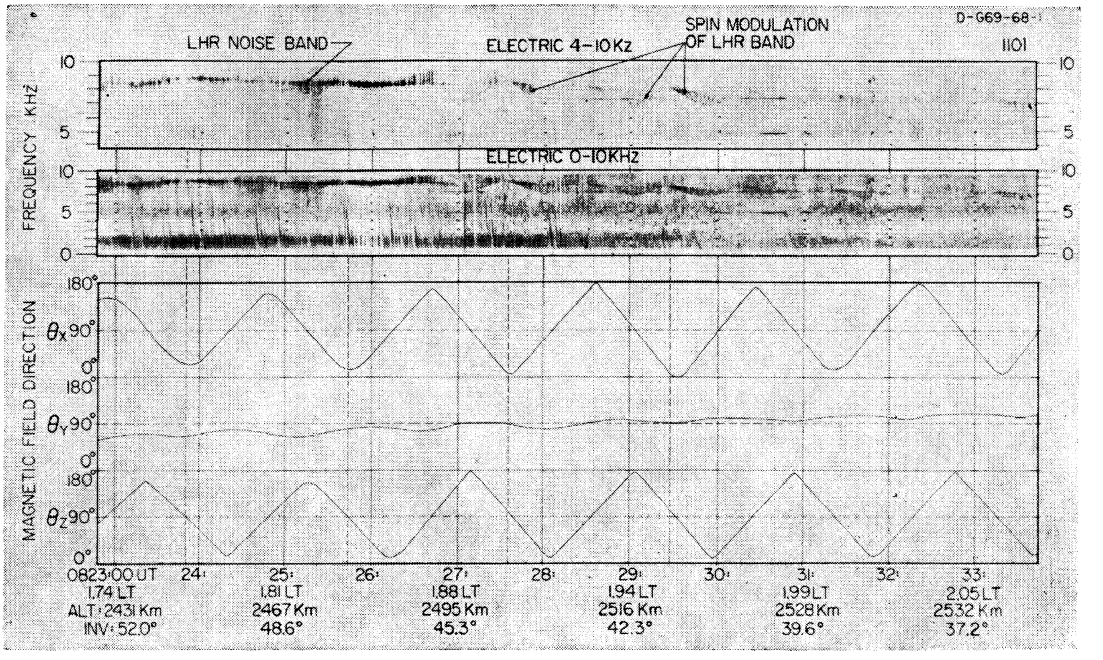

Fig. 12. Spin modulation of lower hybrid resonance noise.

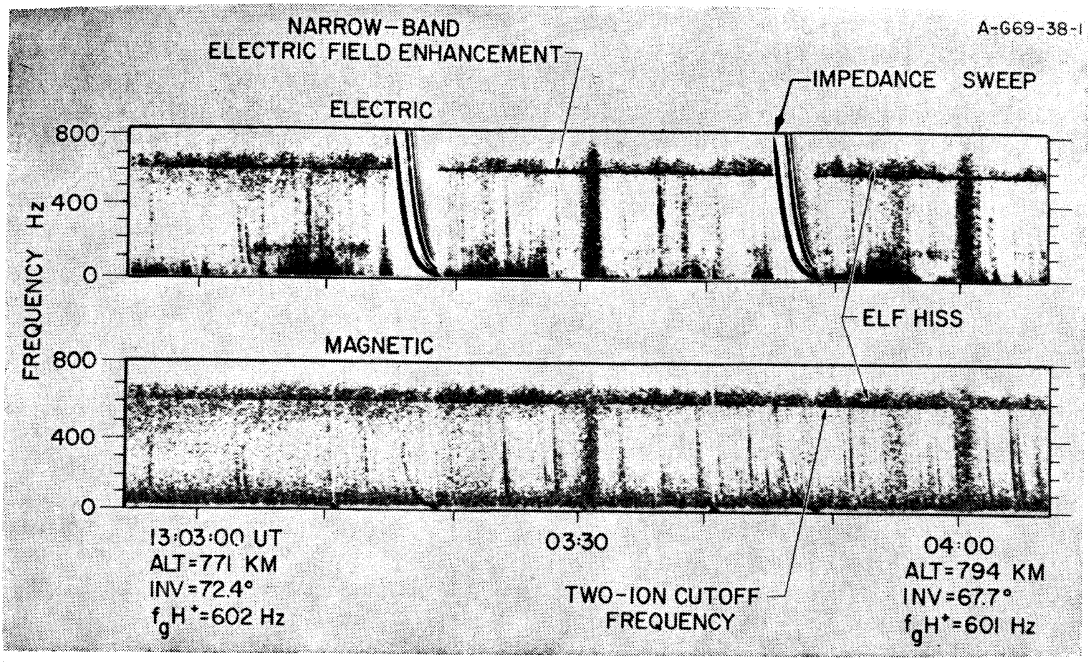

Fig. 13. Electric field enhancement near the two-ion cutoff frequency.

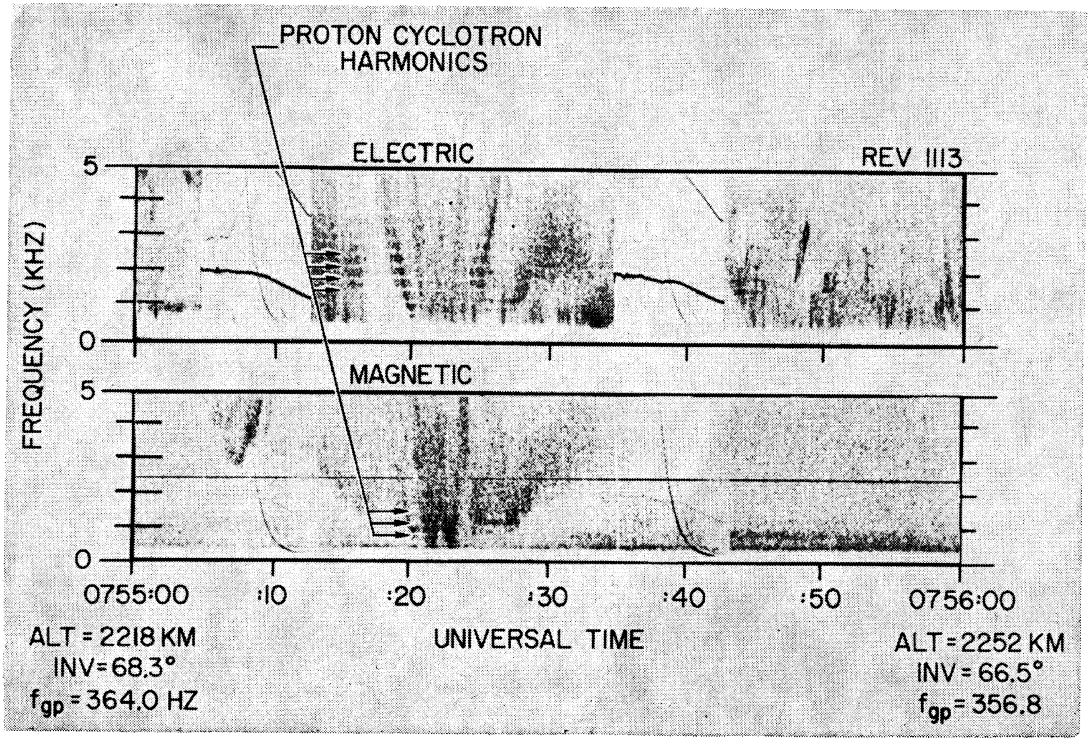

Fig. 14. Proton cyclotron harmonics observed in both the electric and magnetic field frequency spectra.

enhancement near the two-ion cutoff frequency is simply a propagation effect.

C. Proton gyrofrequency harmonics. A new hot plasma phenomena of considerable interest is the observation of proton gyrofrequency harmonics in the frequency spectrum of VLF hiss detected by Injun 5. An example of the proton gyrofrequency harmonic effects observed is illustrated in Figure 14, which shows a series of attenuation bands at harmonics of the proton gyrofrequency. These attenuation bands are most commonly found in the vee-shaped VLF hiss events of the type described by *Gurnett* [1966]. Similar attenuation bands have also been observed on a recent auroral-zone rocket flight [*Mosier and Gurnett*, 1969].

Although the attenuation bands observed are usually most clearly defined in the electric field spectrum, the attenuation bands are also observed in the magnetic field spectrum (see Figure 14). The waves involved in this gyrofrequency harmonic interaction are, therefore, electromagnetic waves.

The center frequencies of the attenuation bands shown in Figure 14 are within about ±50 Hz of the proton gyrofrequency harmonics computed using the *Jensen and Cain* [1962] spherical harmonic expansion for the geomagnetic field at the satellite. In some cases, however, the center frequencies of the attenuation bands are observed to deviate considerably from the gyrofrequency harmonics, sometimes changing in frequency by as much as a hundred Hz in a few seconds. If these observed shifts in the center frequencies of the attenuation bands are caused by Doppler shifts, then the wavelength of the waves being observed must be of the order of 100 meters.

Effects at gyrofrequency harmonics are well known for a hot plasma with a static magnetic field [*Gross*, 1951; *Bernstein*, 1958; *Stix*, 1962; *Crawford*, 1965; *Fredricks*, 1968]. The basic gyrofrequency harmonic interaction mechanism involves an interaction with particles having gyroradii comparable to the component of wavelength perpendicular to the static magnetic field. Propagation effects at harmonics of the electron gyrofrequency have been observed in laboratory plasmas [*Crawford and Weiss*, 1966] and in the ionosphere with the ionospheric sounder on the Alouette satellites [*Calvert and Goe*, 1963; *Fejer and Calvert*, 1964; *Sturrock*, 1965]. Radiation from laboratory plasmas at gyrofrequency harmonics has been reported and studied by several investigators, including *Landauer* [1962], *Bekefi et al.* [1962], *Tanaka and Kubo* [1964], and *Yamamoto and Suita* [1968].

The proton energies involved in the proton gyrofrequency harmonic effects observed with Injun 5 can be estimated from the proton gyrofrequency and the proton gyroradii, which must be comparable to the wavelength of the waves observed. For a typical proton gyrofrequency of 300 Hz and a wavelength (gyroradii) of 100 meters, the proton energies involved are about 150 ev. Intense fluxes of protons with energies of this order have, in fact, been observed with the Injun 5 LEPEDEA experiment coincident with the occurrence of attenuation bands at the proton gyrofrequency harmonics (L. A. Frank, personal communication). A more detailed description of these wave-particle comparisons will be presented in a separate paper.

Acknowledgments. The authors wish to express their thanks to all the personnel involved in the Injun 5 project for their effort in making this experiment a success. We are especially grateful to Dr. J. A. Van Allen, who provided the scientific guidance for the project; to Mr. W. Whelpley, Mr. D. Enemark, Mr. R. Brechwald, and Mr. J. Rogers for their efforts in the design, construction and testing of the spacecraft; and to Dr. S. Shawhan, Mr. J. Cessna, and Mr. D. Odem for their efforts on the VLF experiment. We also greatly appreciate the support from Langley Research Center, particularly from Mr. C. Coffee and Mr. R. Johnson, for assistance in the coordination and management of the project, and from Goddard Space Flight Center for providing telemetry reception and orbit determinations.

This research was supported by the National Aeronautics and Space Administration under contracts NAS5-10625, NAS1-8141, NAS1-8144(F), NAS1-8150(F), and NGR-16-001-043 and by the Office of Naval Research under contract Nonr 1509(06).

References

Barrington, R. E., and J. S. Belrose, Preliminary results from the very-low-frequency receiver aboard Canada's Alouette satellite, *Nature, 198,* 651, 1963.

Bekefi, G., J. D. Coccoli, E. B. Hooper, and S. J. Buchsbaum, Microwave emission and absorption at cyclotron harmonics of a warm plasma, *Phys. Rev. Letters, 9,* 6, 1962.

Brace, L. H., B. M. Reddy, and H. G. Mayr, Global behavior of the ionosphere at 1000 kilometer altitude, *J. Geophys. Res., 72,* 265, 1967.

Brice, N. M., and R. L. Smith, A very-low-frequency plasma resonance, *Nature, 203,* 926, 1964.

Brice, N. M., and R. L. Smith, Lower hybrid resonance emissions, *J. Geophys. Res., 70,* 71, 1965.

Calvert, W., and G. B. Goe, Plasma resonances in the upper ionosphere, *J. Geophys. Res., 68,* 6113, 1963.

Carpenter, D. L., F. Walter, R. E. Barrington, and D. J. McEwen, Alouette 1 and 2 observations of abrupt changes in whistler rate and of VLF noise variations at the plasmapause—a satellite-ground study, *J. Geophys. Res., 73,* 2929, 1968.

Crawford, F. W., Cyclotron harmonic waves in warm plasmas, *Radio Sci., 69D*(6), 789, 1965.

Crawford, F. W., and H. Weiss, Transmission characteristics of cyclotron harmonic waves in a plasma, *J. Nucl. Energy, Pt. C, 8,* 21, 1966.

Fahleson, U., Theory of electric field measurements conducted in the magnetosphere with electric probes, *Space Sci. Rev., 7,* 238, 1967.

Fejer, J. A., and W. Calvert, Resonance effects of electrostatic oscillations in the ionosphere, *J. Geophys. Res., 69,* 5049, 1964.

Frank, L. A., Initial observations of low-energy electrons in the earth's magnetosphere with OGO 3, *J. Geophys. Res., 72,* 185, 1967.

Fredricks, R. W., Structure of generalized ion Bernstein modes from the full electromagnetic dispersion relation, *J. Plasma Phys., 2,* 365, 1968.

Gurnett, D. A., A satellite study of VLF hiss, *J. Geophys. Res., 71,* 5599, 1966.

Gurnett, D. A., Satellite observations of VLF emissions and their association with energetic charged particles, in *Earth's Particles and Fields, Proc. NATO Advanced Study Inst.,* p. 127, Reinhold Publishing Co., New York, 1968.

Gurnett, D. A., and T. B. Burns, The low-frequency cutoff of ELF emissions, *J. Geophys. Res., 73,* 7437, 1968.

Gurnett, D. A., and B. J. O'Brien, High-latitude geophysical studies with satellite Injun 3, 5, Very-low-frequency electromagnetic radiation, *J. Geophys. Res., 69,* 65, 1964.

Gurnett, D. A., S. D. Shawhan, N. M. Brice, and R. L. Smith, Ion cyclotron whistlers, *J. Geophys. Res., 70,* 1665, 1965.

Gross, E. P., Plasma oscillations in a static magnetic field, *Phys. Rev., 82,* 232, 1951.

Helliwell, R. A., *Whistlers and Related Ionospheric Phenomena,* Stanford University Press, Stanford, California, 1965.

Jensen, D. C., and J. C. Cain, An interim geomagnetic field (abstract), *J. Geophys. Res., 67,* 3568, 1962.

Kennel, C. F., and H. E. Petschek, Limit on stably trapped particle fluxes, *J. Geophys. Res., 71,* 1, 1966.

Laaspere, T., M. G. Morgan, and W. C. Johnson, Observations of lower hybrid resonance phenomena on the OGO 2 Spacecraft, *J. Geophys. Res., 74,* 141, 1969.

Landauer, G., Generation of harmonics of the electron-gyrofrequency in a Penning discharge, *J. Nucl. Energy, Pt. C4*(6), 395, 1962.

McEwen, D. J., and R. E. Barrington, Some characteristics of the lower hybrid resonance noise bands observed by the Alouette 1 satellite, *Can. J. Phys., 45,* 13, 1967.

Mosier, S. R., and D. A. Gurnett, Ionospheric observation of VLF electrostatic noise related to harmonics of the proton gyrofrequency, in press, *Nature,* 1969.

Osborne, F. J. F., F. H. C. Smith, R. E. Barrington, and W. E. Mather, Plasma-induced interference in satellite V.L.F. receivers, *Can. J. Phys., 45,* 47, 1967.

Scarf, F. L., R. W. Fredricks, and G. M. Crook, Detection of electromagnetic and electrostatic waves on OV3-3, *J. Geophys. Res., 73,* 1723, 1968.

Smith, R. L., L. Kimura, J. Vigneron, and J. Katsufrakis, Lower hybrid resonance noise and a new ionospheric duct, *J. Geophys. Res., 71,* 1925, 1966.

Stix, T. H., *The Theory of Plasma Waves,* McGraw-Hill Book Company, New York, 1962.

Storey, L. R. O., Antenne electrique dipole pour reception TBF dans l'ionosphere, *L'onde Elec., 45,* 1427, 1965.

Storey, L. R. O., and J. C. Cerisier, An interpretation of the noise bands observed near the lower hybrid resonance frequency by artificial satellites, *Compt. Rend., 266,* 525, 1968.

Sturrock, P. A., Dipole resonances in a homogeneous plasma in a magnetic field, *Phys. Fluids, 8,* 88, 1965.

Tanaka, S., and H. Kubo, Microwave radiation at cyclotron harmonics in a positive column, *Inst. Plasma Phys. Rept. No. 23,* Nagoya University, Nagoya, Japan, 1964.

Taylor, W. W. L., and D. A. Gurnett, Morphology of VLF emissions observed with the Injun 5 satellite, *J. Geophys. Res., 73,* 5615, 1968.

Yamamoto, T., and T. Suita, Excitation of ion cyclotron harmonic waves in a plasma by a perpendicular injected electron beam, *J. Phys. Soc. Japan, 24,* 933, 1968.

(Received April 23, 1969.)